Materials Today Communications 54 (2026) 115667

Contents lists available at ScienceDirect

Materials Today Communications

journal homepage: www.elsevier.com/locate/mtcomm

A pH-triggered hybrid self-healing corrosion protection system utilising UF microcapsules embedded within a biopolymer matrix

Aylin Ahmadinia [a], Carmel B. Breslin [b,*]

[a] Department of Chemistry, Maynooth University, Maynooth, Co., Kildare, Ireland
[b] Kathleen Lonsdale Human Health Institute, Maynooth University, Maynooth, Co., Kildare, Ireland

ARTICLE INFO

Keywords:
pH-triggered release
Self-healing
Corrosion
Urea–formaldehyde microcapsules
Tannic-based epoxy
Controlled release system

ABSTRACT

This study reports a sustainable, pH-responsive microcapsule-based coating for the corrosion protection of iron in a 3.5 wt% NaCl solution. Epoxy and cerium nitrate were encapsulated in microcapsules (UFM) and immobilised in a tannic acid–based epoxy biopolymer (T). The effect of microcapsule levels (0, 1, 3, 6, or 15%) on coating performance was examined. The synthesised microcapsules were characterised using Fourier-transform infrared spectroscopy, X-ray diffraction and thermogravimetric analysis. Morphological features were examined with scanning electron microscopy and optical microscopy, while UV–visible spectroscopy revealed controlled, pH-dependent release of the healing agents, with enhanced release under acidic conditions. Electrochemical tests demonstrated that the coating containing 6% microcapsules exhibited the best corrosion protection, with a low corrosion current density (i_{corr} = 6.13 × 10^{-8} A/cm^2) and a high polarisation resistance (7.55 × 10^4 Ω cm^2). Cyclic polarisation tests revealed a breakdown potential of 0.4 V without any sign of iron dissolution. Using electrochemical impedance spectroscopy, the coating capacitance was determined to be 4.36 × 10^{-11} F. The developed microcapsule-based coating system responded to both pH changes and mechanical damage, providing effective protection for iron. The environmental compatibility of the coating was further assessed by quantifying formaldehyde release using the Nash colourimetric assay. The resulting data confirmed negligible formaldehyde release, supporting the eco-friendly nature of the formulated coating system.

1. Introduction

Corrosion remains a challenge across various sectors, with conventional coatings often failing to provide long-term protection for metallic materials, thereby increasing the demand for smart anti-corrosion coatings [1]. In addition, many traditional coatings contain hazardous chemicals, such as solvents, that pose risks to both the environment and human health. For example, coatings based on volatile organic compounds (VOCs) contribute to air pollution and require strict safety measures. Common coatings such as polyurethane and epoxy, although valued for their strong adhesion and durability, frequently rely on solvent-based formulations that limit their environmental sustainability [2,3]. To address these concerns, increasing attention has centred on green epoxy coatings that eliminate the use of solvents. These sustainable alternatives are often derived from renewable resources and provide improved safety while maintaining effective corrosion protection. Despite advances in these protective coatings, there is a need for smart protection systems capable of inhibiting and repairing damage when it occurs. These systems, also known as self-healing coatings, are designed to perform multiple functions. Their behaviour is generally based on the detection of damage through a stimulus, followed by activation, with the release of protective agents and the repair or restoration of the damaged area [4]. One of the most widely studied triggers for smart coatings on metal surfaces is pH because it is highly effective for corrosion protection and self-healing applications. Once the corrosion event initiates, it is accompanied by a change in pH, making pH an effective trigger [5]. In addition, pH-responsive coatings are versatile and can be combined with other stimuli, enabling controlled encapsulation and release of active agents [6,7]. The active substances primarily include healing agents that repair coating defects and corrosion inhibitors that protect the metal substrate [8].

In many systems, these healing agents or corrosion inhibitors are encapsulated within microcapsules. The core-shell structure of microcapsules typically consists of a polymeric shell enclosing corrosion inhibitors or healing agents. Upon exposure to external stimuli or when cracks form in the coating, the microcapsules rupture and release the

* Corresponding author.
E-mail address: carmel.breslin@mu.ie (C.B. Breslin).

https://doi.org/10.1016/j.mtcomm.2026.115667
Received 22 April 2026; Received in revised form 23 June 2026; Accepted 3 July 2026
Available online 3 July 2026

active materials to inhibit corrosion or repair damaged regions and help restore the integrity of the coating [9]. To date, many types of self-healing microcapsule systems have been developed, consisting of linseed oil [10,11], tung oil [12,13], alkyd resins [14,15], and epoxy–-amine systems [16,17]. Typical shell materials include poly(urea–formaldehyde) [18,19], polyurea [20,21], polyurethane [22,23], and polycaprolactone [24].

Recent studies have focused on bio-based polymers, such as chitosan [25], cellulose [26], and lignin [27], as environmentally friendly alternatives for smart anti-corrosion coatings. These biopolymers can improve coating sustainability while providing additional corrosion protection and self-healing functionality. For example, chitosan coatings containing cerium ions exhibit self-healing and anti-corrosion properties by releasing cerium ions and forming protective cerium hydroxide layers [25]. Among these biopolymers, tannin-based materials have attracted significant attention due to their natural polyphenolic structure, corrosion inhibition ability, and film-forming properties [28]. Tannic acid can interact with metal surfaces through hydroxyl groups, forming protective complexes that inhibit corrosion. Tannic acid has also been loaded into mesoporous silica containers to give self-healing epoxy coatings [29].

The primary objective of this study is to introduce a new class of sustainable pH-responsive urea–formaldehyde microcapsules that contain epoxy as the healing agent and cerium nitrate as a corrosion inhibitor. Both are embedded in a biopolymer that exhibits shape memory effects. This not only inhibits the release of formaldehyde, but also contributes to the healing of defect sites or corrosion sites. Urea-formaldehyde microcapsules in self-healing coatings can pose environmental and health risks due to potential release of formaldehyde [30]. Therefore, employing green and sustainable polymer matrices that can trap formaldehyde is needed to minimise its release into the environment while ensuring effective corrosion protection.

Cerium was selected because it is well known to provide self-healing corrosion protection and, when released, acts as an effective inhibitor by forming $Ce(OH)_3$ at corrosion sites. Indeed, cerium nitrate has been encapsulated in pH-sensitive poly(melamine–formaldehyde) microcapsules for corrosion inhibition [31–34]. Unlike previous pH-sensitive poly (melamine–formaldehyde) systems, this design integrates both a crack-sealing epoxy phase and an active cerium-based inhibitor within a single microcapsule, enabling synergistic protective responses. This system exhibits a hybrid self-healing mechanism. The microcapsules release the epoxy healing agent and cerium inhibitor upon corrosion, while internally, the shape memory biopolymer aids crack closure. The released epoxy can also undergo crosslinking and polymerisation, aiding the healing step. Together, these inhibition mechanisms inhibit iron corrosion, highlighting the unique properties of this multifunctional capsule–biopolymer system. This approach not only enhances the durability and performance of iron-based materials but also promotes a new, sustainable, and environmentally friendly method for developing smart corrosion-protective coatings.

2. Experimental

Details of the chemicals employed and the equipment used in the characterisation and electrochemical measurements are provided in the supplementary data.

2.1. Synthesis of urea-formaldehyde microcapsules loaded with epoxy and cerium nitrate (UFM)

Urea-formaldehyde microcapsules (UFM) were synthesised utilising an in situ polymerisation technique. A solution was prepared by dissolving 5 g of NaCl, 5 g of urea, 0.5 g of NH_4Cl, and 0.5 g of resorcinol in 250 mL of deionised water. This mixture was mechanically stirred at 420 rpm. SDBS at a concentration of 2 wt%, was then incorporated into the solution, and the pH was adjusted to 3.5. A mixture of epoxy resin (1 g) and $CeNO_3$ (0.03 g) was then added dropwise and stirred for an additional 30 min until the composite droplets were well dispersed in the solution. Following this, 12.6 g of formaldehyde was added to the emulsion, and the mixture was heated to 70 °C, allowing the reaction to proceed for approximately 2 h, during which white microcapsules began to form. Finally, the synthesised microcapsules loaded with epoxy and cerium nitrate (UFM) were filtered and dried at room temperature for 24 h. This microencapsulation process is illustrated in Scheme 1.

2.2. Synthesis of tannic-derived epoxy (T)

Initially, 10 g of tannic acid was dissolved in 100 mL of 0.5 M NaOH under mechanical stirring, then transferred to a 250 mL round-bottom flask. Subsequently, epichlorohydrin was added dropwise at 40 ° C. The reaction mixture was subsequently heated to 65 °C, at which point the pH was adjusted to 7.5 by adding drops of NaOH. The reaction was refluxed at 80 °C for 2–3 h until a dark brown product was formed. The resultant resin was then transferred to a separating funnel, and the aqueous phase was decanted. The resin was washed thoroughly with water three times to ensure purification. Finally, the resin was dissolved in THF to remove any unreacted species and dried in a rotary evaporator.

2.3. Coating development

Initially, iron electrodes with a surface area of 0.07 cm^2 were polished with 1200-grit SiC abrasive paper, then thoroughly cleaned with ethanol and water. To formulate the microcapsule-based coating system, various concentrations of the UFM microcapsules (0, 1, 3, 6, or 15 wt% relative to the bio-epoxy matrix) were systematically incorporated into the tannic-derived epoxy matrix to give a coating thickness of 0.70 ± 0.05 mm at the iron, as presented in Table 1. Subsequently, the coatings deposited on the iron electrode were dried under an infrared lamp for 1 h to remove moisture from the resin matrix and ensure structural stability. The coating thickness was controlled by preparing three samples under the same coating and curing conditions. The thickness was measured using a USB microscopic device at three different spots on each coating surface, and the average value was reported. According to ASTM D3359, a standard tape adhesion test with 180° pull-off was performed to evaluate the coating adhesion to the iron substrate. Eleven cuts with 1 mm spacing were made, followed by tape application and removal after 60 s. No coating delamination or removal was observed.

The environmental compatibility of the coating was further assessed by quantifying formaldehyde emissions using the Nash colourimetric assay (based on the Hantzsch reaction between formaldehyde, acetylacetone, and ammonia) in accordance with ASTM D5910. Standard calibration curves were prepared using formaldehyde concentrations of 0.05, 0.1, 0.2, and 0.3 mg/L after reaction with Nash reagent. The sample solutions were reacted with the Nash reagent, heated at 50 °C for 15 min, and then cooled to room temperature before UV–Visible analysis. The absorbance of the samples was measured at 412 nm.

2.4. Control release studies

The release of cerium ions from the coating was monitored using UV–visible spectroscopy (Cary 50 UV–visible spectrometer) by complexing the cerium ions with alizarin red. Initially, calibration curves were generated at different pH values using cerium nitrate at concentrations of 1, 3, 6, and 9 mg/mL. Alizarin red S (ARs) at a concentration of 1 mM was used to complex cerium at pH values of 4, 7, and 10. The release of cerium from the microcapsules within the biopolymer matrix was then monitored as a function of pH (4, 7, and 10) and over time intervals of 24, 48, and 72 h. All samples were diluted with 15 mL of deionised water after mixing the cerium-containing solution and ARs solution in a 1:1 (volume) ratio.

To further analyse the released fraction and the amount of residual

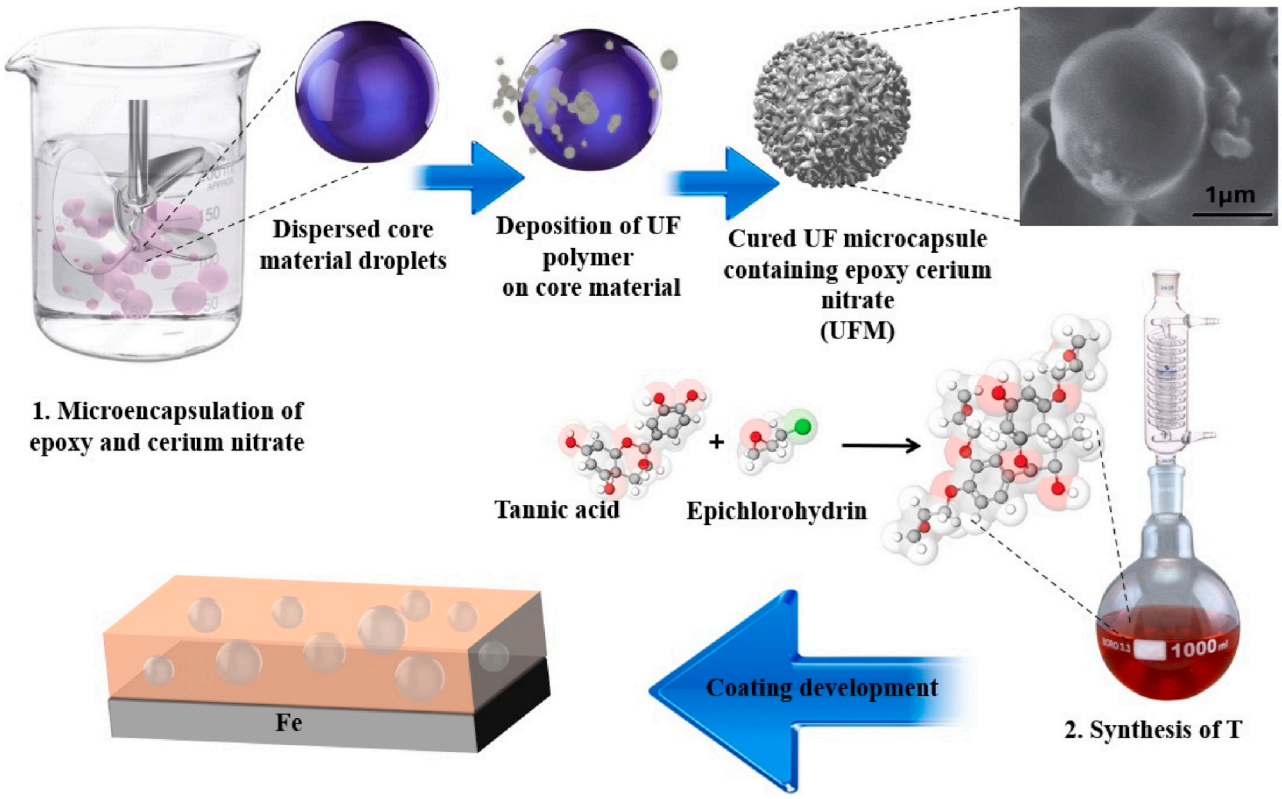

Scheme 1. Illustration of the formation of the epoxy and cerium, their encapsulation in urea-formaldehyde, the formation of the tannic-derived epoxy, T, and the final coating comprising the UFM immobilised within T.

Table 1
Summary of composition of the T and UFM and sample codes.

Sample Code	(T) (g)	UFM (g)
T-UFM−0	1	0
T-UFM−1	1	0.01
T-UFM−3	1	0.03
T-UFM−6	1	0.06
T-UFM−15	1	0.15

cerium inhibitor within the UFM, the encapsulation efficiency was determined using Eq. 1. Here, W_i and W_f refer to the initial and final weights, corresponding to the weight of the UFM and the weight of the capsule on removing its contents. In a typical analysis, 67.2 mg of UFM was weighed out and ground to break up the microcapsules. This sample was then washed 3 times with acetone to dissolve the core epoxy and cerium nitrate. Then the residue was dried to give W_f, representing the shell material without its contents. Using this approach, the encapsulation efficiency was determined to be 80%.

$$\text{Encapsulation efficiency} = (1 - W_f/W_i) \times 100 \quad (1)$$

Based on this analysis, the core content of the coatings was calculated to be 0.144, 0.432, 0.864, and 2.16 mg of cerium nitrate (CeN) for T-UFM−1, T-UFM−3, T-UFM−6, and T-UFM−15, respectively.

3. Results and discussion

3.1. Characterisation studies

Morphological analysis was performed using scanning electron microscopy (SEM), and representative micrographs are presented in Fig. 1. The UFM, containing the epoxy and cerium nitrate, consists of closely packed, nearly spherical particles with a relatively narrow size range, as shown in Fig. 1(a). The surfaces of the individual particles appear smooth and well-defined. At higher magnifications, Fig. 1(b), some irregularities, including the presence of small particles on the surface of the microcapsules, are evident, likely resulting from unreacted monomers. The spherical particles have diameters ranging from 0.6 to 1.6 µm, as indicated in the histogram in Fig. 1(e). Most particles are approximately 0.7–1.1 µm in diameter, with an average particle size of about 0.86 µm, as indicated on the plot. This confirms that the microcapsules are predominantly composed of sub-micrometre to micrometre-sized particles with only a small fraction of larger particles.

The T matrix, utilised to host the UFM, exhibits a rough morphology with a non-uniform particle-size distribution. In the higher-magnification SEM image in Fig. 1(c), the material appears as irregularly shaped structures and agglomerates composed of smaller-sized particles. These agglomerates exhibit a broad range of sizes extending to a few hundred micrometres. This irregular structure extends over the surface, as evident at lower magnification in Fig. 1(d). In Fig. 1(f, g), T-UFM−6 shows an even distribution of microcapsules throughout the biopolymer matrix. The microcapsules maintain their shape during mixing, indicating good stability and uniform dispersion.

In Fig. 2(a), the FTIR spectra, recorded for the T, the UFM and the composite T-UFM−6, are presented. The broad absorption bands observed in the range of 3300–3500 cm^{-1}correspond to the stretching vibrations of hydroxyl and amine groups within the urea-formaldehyde. Notably, this broad peak shows increased intensity for the UFM containing cerium nitrate, indicating the presence of water molecules within hydrated cerium nitrate that contribute additional hydroxyl groups detectable in this spectral region. Peaks specific to urea-formaldehyde are identified around 1500–1600 cm^{-1}, with characteristic peaks at 550 cm^{-1} (N–H), 1640 cm^{-1} (C═O), and 3330–3350 cm^{-1} (N–H and O–H) in good agreement with previous studies [35]. The terminal epoxide group is seen at 830 cm^{-1} [36]. Additional peaks at 1125 cm^{-1} and 1168 cm^{-1} correlate with C-OH vibrations, and small

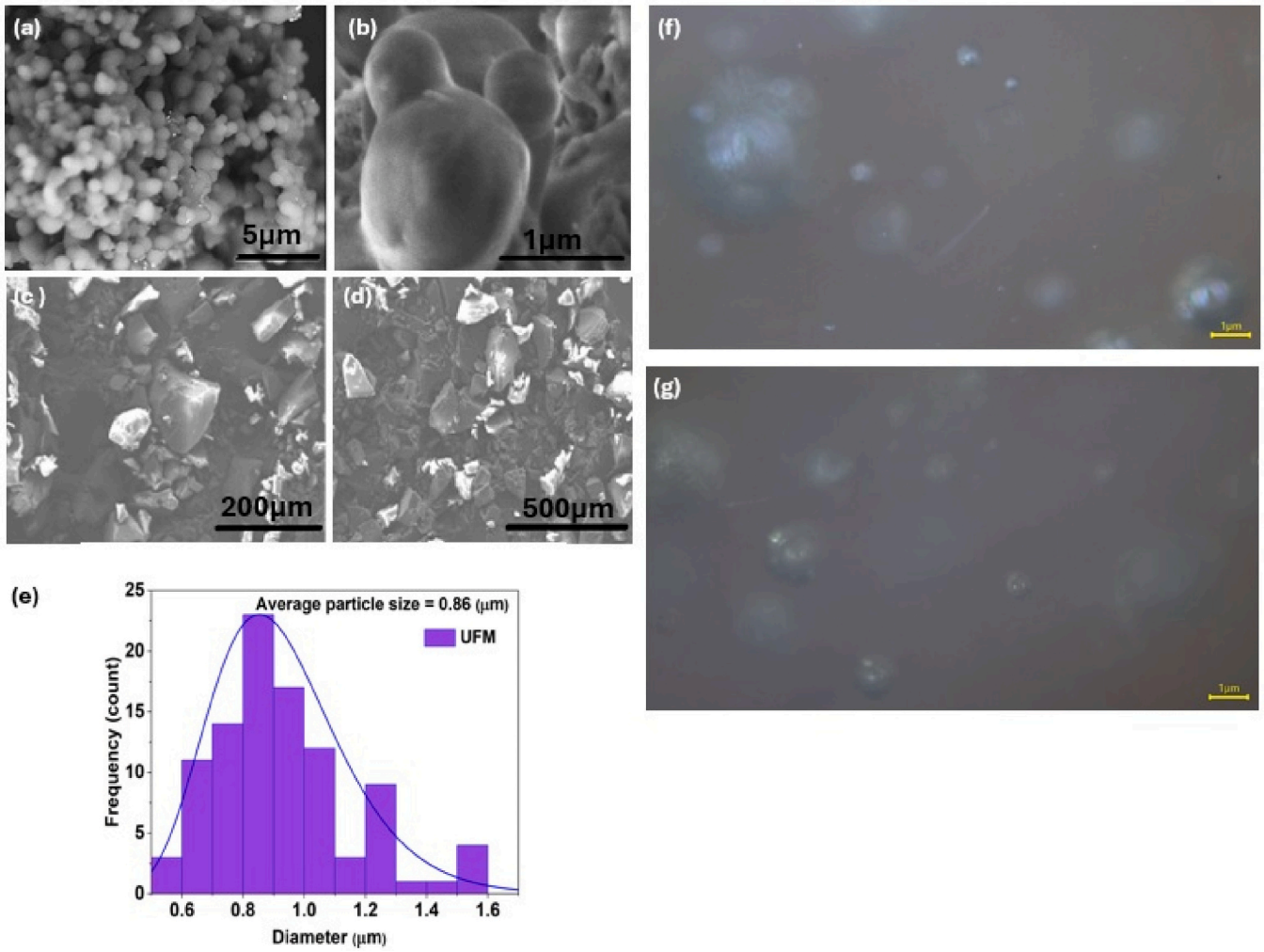

Fig. 1. The SEM images of (a, b) UFM, (c, d) T and (e) particle size distribution of UFM, and (f, g) optical microscopy images showing the distribution of microcapsules in T-UFM−6.

peaks near 1200 and 1300 cm^{-1} confirm the presence of C-N bonding in the UFM [37,38]. The peak at approximately 1560 cm^{-1} indicates the N-H group, while the presence of C═O bonding is denoted by a peak at 1629 cm^{-1}. Sharper peaks near 1600 cm^{-1} are associated with the incorporation of cerium nitrate in the UFM [35].

The presence of tannins or phenolic compounds within T is evidenced by a broad peak ranging from 3000 to 3600 cm^{-1}, centred around 3275–3330 cm^{-1}, which corresponds to the phenolic hydroxyl group [39,40]. Peaks in the 1000–1275 cm^{-1} range confirm the presence of C-H bending modes, while the bands between 600 and 800 cm^{-1} demonstrate C-C bond deformation within the aromatic skeleton, with absorption observed at 1500–1570 cm^{-1}. These findings align with previous studies highlighting that the epoxidation of tannins alters peak positions, with peaks at 920 cm^{-1} and 673 cm^{-1}, indicating the presence of epoxy rings in tannic-based epoxy [39]. For the composite containing 6% UFM, the FTIR spectra indicate that the positions and intensities of the T peaks, both in isolation and in the presence of UFM, are very similar, consistent with the relatively low concentration of UFM.

The XRD analysis reveals that both components, T and UFM, exhibit a mix of amorphous and crystalline structures. The prominent peaks are located at nearly the same position and correspond to the amorphous epoxy composite, specifically at around 2θ of 20° (111) [41,42]. These peaks are characteristic of the epoxy present in both the T and the UFM microcapsules. Notably, the peak intensity for the T is greater than that for the UFM, due to the encapsulation of relatively small amounts of epoxy within the UF shell. The XRD pattern of tannic acid shows amorphous features with broad peaks at approximately 28.5° and 40° [43]. However, when combined with the epoxy, the structure exhibits more crystalline behaviour, with peaks at 20.8° and 45.6°. This shift in peak position is attributed to the epoxidation of tannic acid [44–46]. The XRD patterns for UFM also show a combination of amorphous and crystalline phases. Although research on the UFM structure is limited, it is known that crystallinity is influenced by the formaldehyde-to-urea (F/U) ratio. A higher F/U molar ratio tends to yield an amorphous structure with peaks near 21.0° and 31.5° [47,48]. In this study, the overlapping broad peaks of the epoxy (core material) and UFM (shell material) around 20° exhibit lower intensity in the UFM microcapsules. Additionally, peaks near 45° (311) and 56° (400) are associated with the crystalline structure of cerium nitrate incorporated into the core of the UFM [49].

The thermal stabilities of UFM, T, and the composite, T-UFM−6, were studied using TGA and the corresponding data are shown in Fig. 2 (c). The temperature was varied from room temperature to 700 °C. The UFM sample exhibits a multi-step weight loss, with the first step at about 100 °C, reflecting the removal of adsorbed water molecules from the UFM shells. This is followed by the decomposition of less-stable organic components at higher temperatures, combined with the loss of water from the cerium nitrate salt within the UFM shells. This initial weight loss is due to the evaporation of physically adsorbed water and does not

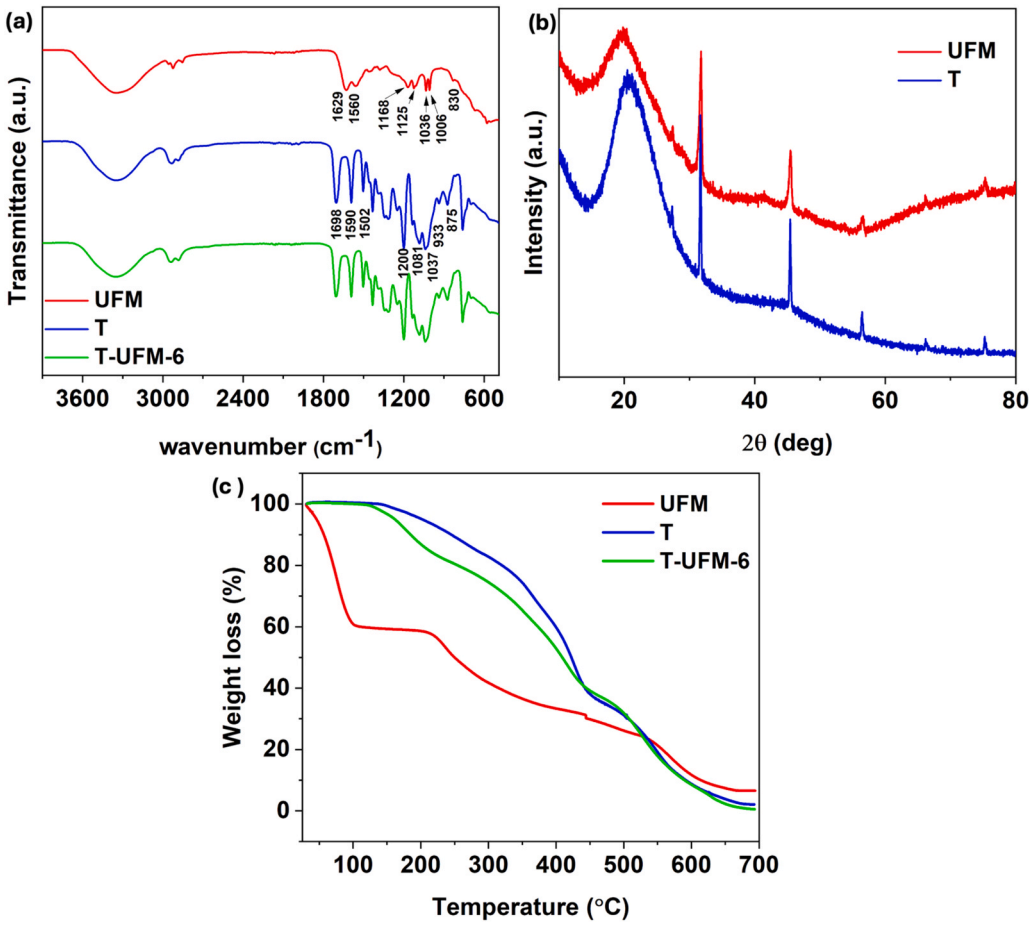

Fig. 2. (a) FTIR, (b) XRD, and (c) TGA data recorded for UFM, T and T-UFM−6.

involve chemical degradation, showing that the microcapsule shell remains stable at this stage. The subsequent weight loss observed at about 250 °C is consistent with the degradation of the urea-formaldehyde shell material. This degradation involves the breaking of methylene (–NH–CH_2–NH–) and ether bridges in good agreement with previous studies [50,51]. The final weight loss is linked to epoxy degradation, which commences at about 350 °C [52].

Both T and T-UFM-6 show more gradual weight-loss behaviour and retain a significantly higher residual mass at elevated temperatures, indicating improved thermal stability. The similarity between the T and T-UFM-6 curves suggests that the structural changes responsible for the stability mainly occur due to the T component. The T matrix likely promotes additional crosslinking and hydrogen-bonding interactions, which restrict polymer chain mobility and delay the onset of thermal bond cleavage. There is minimal weight loss near 100 °C, indicating few adsorbed water molecules. For the T, degradation commences at about 200 °C, with approximately 20% weight loss observed by 350 °C. A more substantial degradation with about a 60% loss occurs at 450 °C, reflecting very good thermal resistance. Notably, earlier research has indicated that significant degradation of tannic acid occurs around 250 °C [53]. This is not evident, suggesting that the tannic acid is effectively integrated within the T matrix. This integration likely suppresses the independent thermal decomposition of tannic acid by stabilising it through intermolecular interactions within the matrix. The weight loss of the T-UFM-6 is somewhat higher, consistent with the presence of the UFM.

3.2. Electrochemical and corrosion studies

To evaluate the effectiveness of UFM, T and the T-UFM composites, the potentiodynamic polarisation technique was employed. Various coating formulations were prepared by incorporating UF microcapsules containing epoxy and cerium nitrate (0, 1, 3, 6, and 15%) into T, as shown in Table 1. The coatings were applied to the iron substrate and immersed in 3.5 wt% NaCl solution for time intervals of 1 h and 24 h before the electrochemical tests. Polarisation curves recorded at 1 mV/s are shown in Fig. 3(a). In the Tafel plots, the influence of the concentration of the cerium corrosion inhibitor immobilised within the UFM is shown. Pure iron has the lowest E_{corr} (corrosion potential) and the highest i_{corr} (corrosion current density). With the T coating applied but without the UFM (T-UFM−0), the i_{corr} is lower than that of the uncoated iron. Notably, the introduction of 3% microcapsules to give T-UFM−3, results in a marked reduction of the i_{corr} relative to the unmodified electrode and an increase in the E_{corr}. The T-UFM−6 formulation incorporating 6% microcapsules demonstrates the optimal performance, exhibiting significant enhancement in corrosion resistance compared to the bare iron, Fig. 3(b). Both the anodic and cathodic branches of the Tafel plots are markedly suppressed for T-UFM-6 relative to bare Fe, indicating mixed-type corrosion inhibition. However, the shift in E_{corr} to higher values indicates a greater decrease in the rate of the reduction reaction. This is consistent with a compact layer that inhibits both iron oxidation and the oxygen reduction reaction or hydrogen evolution reaction. However, increasing the microcapsule concentration to 15% compromised the structural integrity of the coating, likely leading to increased porosity and the formation of pathways that facilitate the ingress of corrosive ions and water molecules. For comparison, data recorded at a lower scan rate of 0.166 mV/s are shown in Figure S1 and Table S1 (supplementary data). This comparison shows the same trends but with somewhat lower currents, as expected under near-steady-state conditions. The uncoated iron exhibits higher i_{corr}, whereas all coated

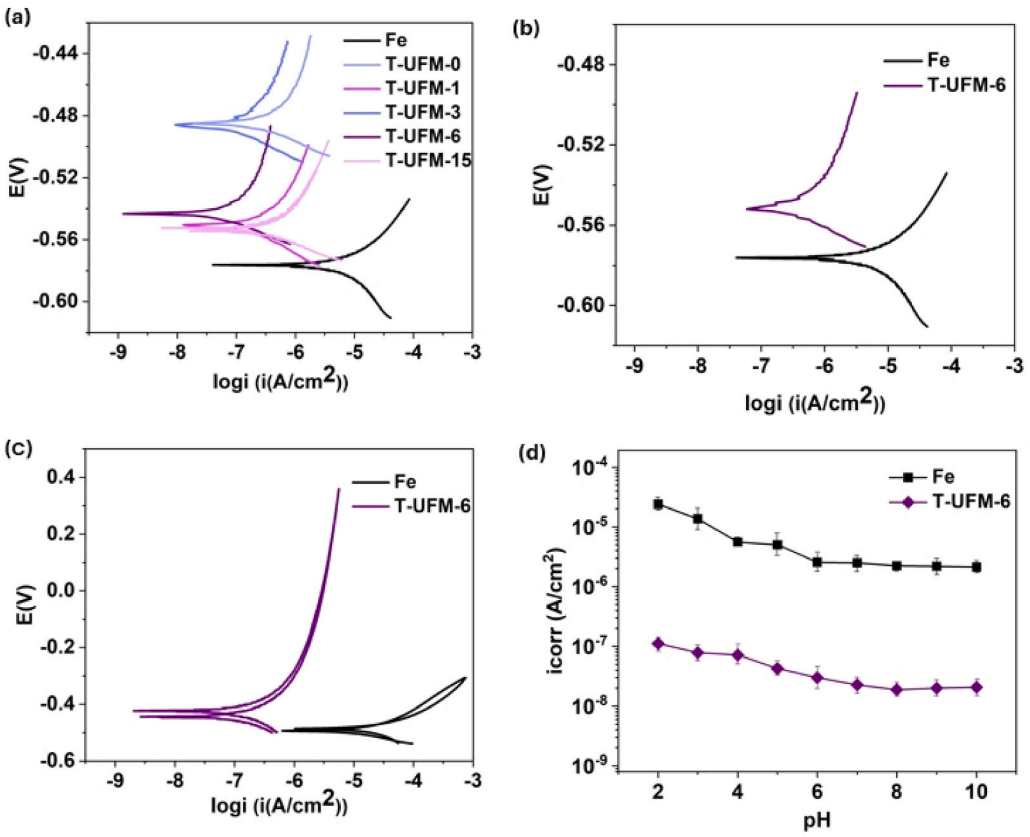

Fig. 3. Tafel curves recorded for T-UFM-modified iron and pure iron following (a) 1 h and (b) 24 h immersion in NaCl, (c) cyclic potentiodynamic polarisation curves for Fe and T-UFM−6, (d) i_{corr} of Fe and T-UFM−6 as a function of pH (n = 3).

samples show lower values. T-UFM−6 and T-UFM−3 provide the greatest corrosion protection, with T-UFM−6 being the optimal coating with the lowest i_{corr}.

Cyclic potentiodynamic polarisation curves were recorded at a scan rate of 1 mV/s in a 3.5% NaCl solution, and typical data are shown in Fig. 3(c). With this extended potential window, active iron dissolution occurs, whereas T-UFM-6 maintains low currents over a much broader potential range, consistent with the development of a highly stable coating. As shown in Fig. 3(c), the potential can be increased up to approximately 0.4 V without signs of iron dissolution. Additionally, when the potential is reversed, the current remains low, and there is minimal hysteresis, suggesting no significant corrosion of the substrate. These results clearly demonstrate the strong corrosion resistance provided by the T-UFM−6 coating.

The corrosion protection capacity of the optimal T-UFM-6 coating system was monitored over a large pH range. The potentiodynamic technique, shown in Fig. 3(a), was performed at pH values ranging from 2 to 10 after a 1-h immersion in the aggressive solution. In Fig. 3(d), the extracted i_{corr} is plotted as a function of the pH of the solution. For pure iron, i_{corr} decreases slightly as pH increases, consistent with iron behaviour, where corrosion is more severe in acidic solutions and less aggressive in near-neutral to mildly alkaline media. When the iron electrode is modified with T-UFM-6, i_{corr} decreases by two to three orders of magnitude across the entire pH range, indicating that the coating effectively protects the iron substrate. This wide pH tolerance indicates that T-UFM-6 forms a dense coating that maintains high inhibition efficiency across both acidic and alkaline conditions, which is beneficial for practical applications where local pH levels can vary.

The experimental data were further analysed to determine the polarisation resistance (R_p) using Eq. 2. In this equation, b_a and b_c are the anodic and cathodic Tafel constants, respectively. The calculated parameters are summarised in Table 2, which clearly indicates that the T-UFM−6 coating offers the highest R_p and the lowest i_{corr}.

$$R_p = \frac{1}{2.303 i_{corr}\left(\frac{1}{b_a}+\frac{1}{b_c}\right)} \quad (2)$$

Electrochemical impedance spectroscopy (EIS) was employed to characterise the corrosion resistance of the optimal coating system, T-UFM−6, in a 3.5 wt% NaCl solution. EIS measurements were conducted over a frequency range of 0.01 Hz to 100,000 Hz. Typical data observed after a 30-min immersion period are presented in Fig. 4(a), with Bode

Table 2
Summary of corrosion parameters derived from the Tafel curves.

	E_{corr} (mV)	R_p (Ω cm^2)	b_a (mv/dec)	b_c (mv/dec)	i_{corr} (A/cm^2)
Fe	−576	1.10×10^3	21.07	32.69	$5.04 \pm 0.25 \times 10^{-6}$
T-UFM−0	−485	1.91×10^4	37.30	18.09	$2.76 \pm 0.38 \times 10^{-7}$
T-UFM−1	−550	2.83×10^4	27.97	24.27	$1.99 \pm 0.45 \times 10^{-7}$
T-UFM−3	−486	5.03×10^4	45.01	27.47	$1.47 \pm 0.38 \times 10^{-7}$
T-UFM−6	−543	7.55×10^4	29.18	16.80	$6.13 \pm 0.28 \times 10^{-8}$
T-UFM−15	−552	1.19×10^4	19.29	12.13	$2.71 \pm 0.08 \times 10^{-7}$

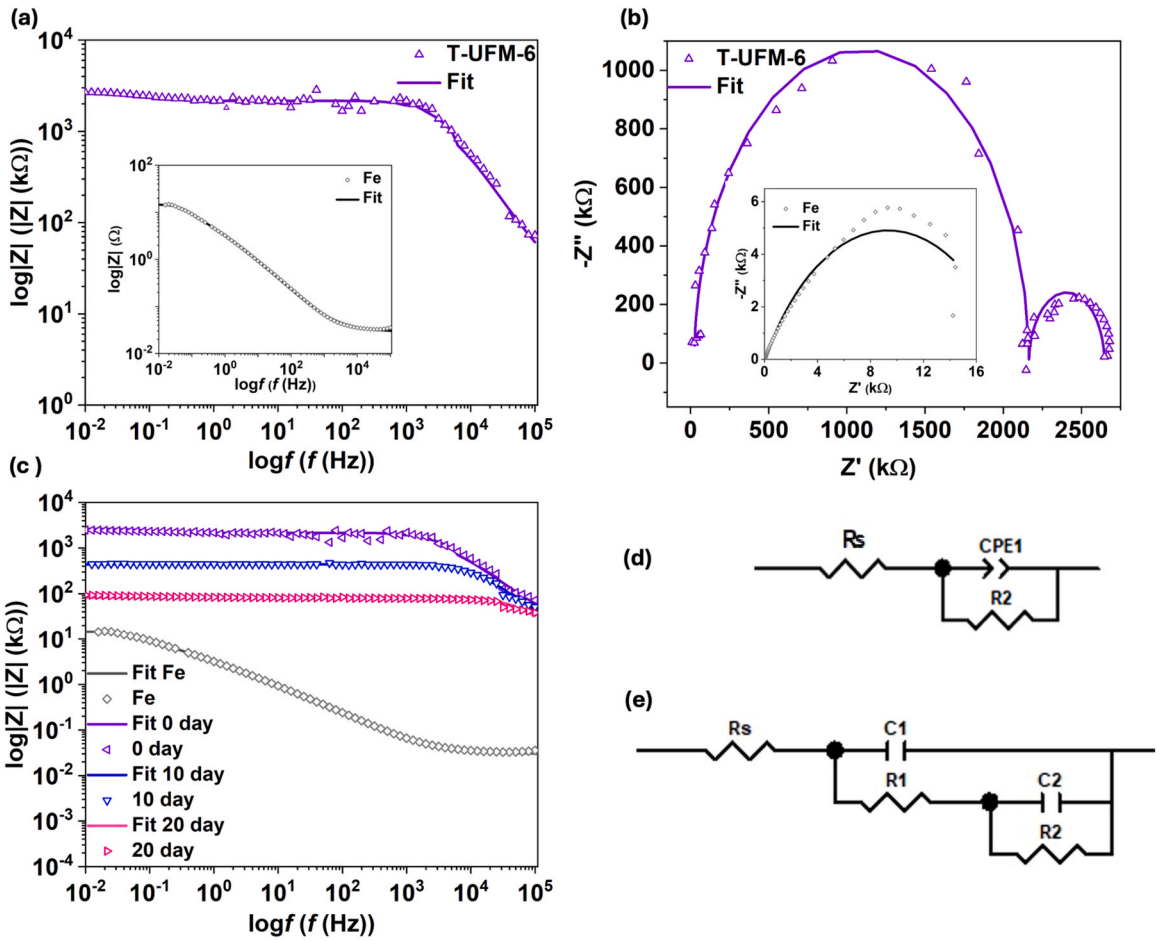

Fig. 4. EIS measurements **(a)** logarithm of |Z| as *a* function of frequency for T-UFM−6 modified iron with inset showing the response of pure iron, **(b)** corresponding Nyquist plots, and **(c)** impedance response as a function of time, recorded at pH of 7.0 in 3.5 wt% NaCl, and **(d,e)** circuits used in fitting impedance data. The continuous traces represent the simulated data from circuit fitting, while the symbols indicate the experimental data.

plots showing impedance as a function of frequency for pure iron and the T-UFM−6-modified iron. The Bode plot recorded for the T-UFM−6 coating reveals a high impedance modulus of 2.12×10^3 kΩ over a broad frequency range, indicating a highly resistive and capacitive barrier to electrolyte penetration, characteristic of high-performing coatings. The corresponding Nyquist plot, depicted in Fig. 4(b), displays a large, depressed semicircle and a smaller one at lower frequencies, confirming that the electrochemical response is dominated by two time constants. The insets compare the impedance response of bare Fe, which exhibits much lower impedance and a significantly smaller semicircle, highlighting the substantial improvement in charge-transfer resistance imparted by the T-UFM-6 coating.

The equivalent electrical circuit was selected, as shown in Fig. 4(d) and (e), according to the features observed in the Nyquist and Bode plots. For T-UFM−6, the Nyquist spectrum shows two capacitive loops, indicating two electrochemical processes with different time constants. Therefore, the data were fitted using $R_s - (R_1\|C_1) - (R_2\|C_2)$, where R_s is the solution resistance, $R_1\|C_1$ represents the response of the protective coating layer, and $R_2\|C_2$ represents the charge-transfer process at the coating/iron interface. In contrast, the response of bare Fe is better modelled using a constant phase element, with R_s–$(R_2\|CPE_1)$ as the circuit. The elements R_2 and CPE_1 correspond to the charge-transfer resistance and double-layer capacitance at the metal/electrolyte interface, respectively, where the constant phase element accounts for the non-ideal capacitive behaviour arising from the corrosion reactions at the uncoated iron surface. Using these equivalent circuits, the charge-transfer resistance was computed to be 18.6 ± 0.2 kΩ for pure iron, but was much higher at $2.12 \pm 0.03 \times 10^3$ kΩ for the T-UFM−6-modified iron. This high resistance was accompanied by a low capacitance of $2.67 \pm 0.02 \times 10^{-11}$ F, consistent with a highly protective coating. This confirms that the T-UFM−6 coating strongly suppresses corrosion reactions. These measurements compare favourably with some recent studies, in which the charge-transfer resistance values of the coatings are in the 10^4–10^6 Ω region [9,54].

The second capacitance term (C_2) has a value of $3.5 \pm 0.04 \times 10^{-6}$ F, and the corresponding R_2 is 51 ± 0.04 kΩ. This suggests some electrolyte penetration and possible hydration of the iron-coating interface. In this pH-responsive system, such electrolyte penetration can help trigger the release of the encapsulated healing agent. Despite the higher C2, the high charge-transfer resistance indicates that the coating still provides good corrosion protection.

Further studies were carried out using EIS, over a 20-day period, and these data are presented in Fig. 4(c). Initially, the impedance is high at 2.12×10^3 kΩ, but it decreases with increasing immersion, reaching 3.94×10^2 kΩ after 10 days of immersion. This gradual decrease in impedance at lower frequencies with immersion time suggests water uptake and the onset of minor defect formation within the film. However, even after 20 days of immersion, the impedance of the coated samples remains several orders of magnitude higher than that of bare Fe, indicating that the coating preserves an effective barrier and minimizes corrosion processes at the metal/coating interface.

The self-healing capacity of the optimised T-UFM-6 coating was evaluated using a combination of EIS and optical imaging after a defect was introduced into the coating. Following 24 h of immersion in the

chloride-containing solution, the surface was mechanically scratched with a razor blade to generate the defect and activate the microcapsule-based self-healing system. The impedance was monitored over an additional 4-day immersion period to assess its self-healing capability. Prior to scratching, the initial impedance was high, as shown in Fig. 5(a), indicating the presence of a protective coating. Following the formation of the defect, the impedance decreases significantly, consistent with corrosion at the defect. A slight increase in impedance was observed on the second day of immersion, attributed to the release of healing agents from the microcapsules and subsequent crack sealing. Previous studies have reported that cerium salts can promote epoxy polymerization and ring-opening reactions, acting as curing catalysts or curing promoters [55,56]. Therefore, besides forming a protective cerium hydroxide/-oxide passivation layer on the metal surface, the released Ce^{3+} ions may also facilitate local crosslinking of the released epoxy within the damaged region, thereby healing the damaged coating. The impedance value further increases substantially on the third day, confirming the healing ability. Light microscopy images supported these findings, showing the initiation of the healing process on the second day and the disappearance of the cracked region by the third day, as illustrated from the comparison of Figs. 5(b) and 5(c), thereby demonstrating the effective sealing of the damaged site by the contents released from the microcapsules. This is further illustrated in Figs. 5(d), 5(e) and 5(f), which highlight the progressive healing of the damaged site.

To determine whether the cerium hydroxide passivation layer forms at the corrosion site, an additional experiment was designed. The scratched T-UFM−6 coating was immersed in 3.5 wt% NaCl solution for 3 days. After this immersion period, the coating was removed, rinsed with deionised water, dried, and the scratched region on the iron substrate was analysed using FTIR to investigate the formation of the cerium hydroxide layer after healing and the release of Ce^{3+} ions into the medium. The FTIR results, shown in Figure S2, revealed a broad band at 3000–3600 cm^{-1} , corresponding to hydroxyl groups, indicating the formation of hydroxide species. A sharp peak around 550 cm^{-1} was attributed to the Ce-O bond, confirming the formation of cerium hydroxide/oxide compounds on the metal surface. Peaks observed in the 2100–2400 cm^{-1} region were attributed to aromatic C–H stretching of the tannic acid-based matrix, likely due to residual coating residues left after peeling. In addition, no peak was detected in the 900–915 cm^{-1} region, indicating that the epoxy compound was not released directly onto the metal surface.

To complement these healing studies, an elevated temperature was used. The scratched coated samples were immersed in a 5 wt% NaCl solution at 35 ± 2 ℃ for 3 days, and digital images of the healing process were collected, as illustrated in Figure S3. After healing, the scratch lines are largely filled and bridged by the coating. The continuity of the barrier layer is effectively restored, demonstrating the ability of the coating to repair defects and re-establish protection of the iron substrate. These results clearly show the self-healing capability and durability of the coating, without any blistering or delamination after immersion, even at this elevated temperature.

To gain further insight into the release rate of the cerium corrosion inhibitor and the residual concentration remaining in the UFM capsules, a spectrophotometric study was conducted. Firstly, the influence of pH on the release of cerium nitrate from the UFM immobilised in the T matrix was monitored over 24, 48, and 72 h, at pH 4, 7, and 10. Typical data are shown in Fig. 6(a) and (b), which illustrate the controlled-release profile of the cerium inhibitor from various T-UFM coatings, demonstrating their pH-responsive and time-dependent behaviours.

At pH 7.0, the T-UFM−15 exhibits the highest release, increasing from approximately 0.006 mg/mL at 24 h to 0.007 mg/mL at 48 h, indicating sustained high release over 48 h. However, this release rate decreases over longer times. On the other hand, T-UFM−1 showed the lowest release rate with a more sustained release over 72 h, whereas T-UFM−3 and T-UFM−6 released somewhat higher amounts of the cerium inhibitor. The T-UFM−6 exhibits a moderate, stable, and well-balanced

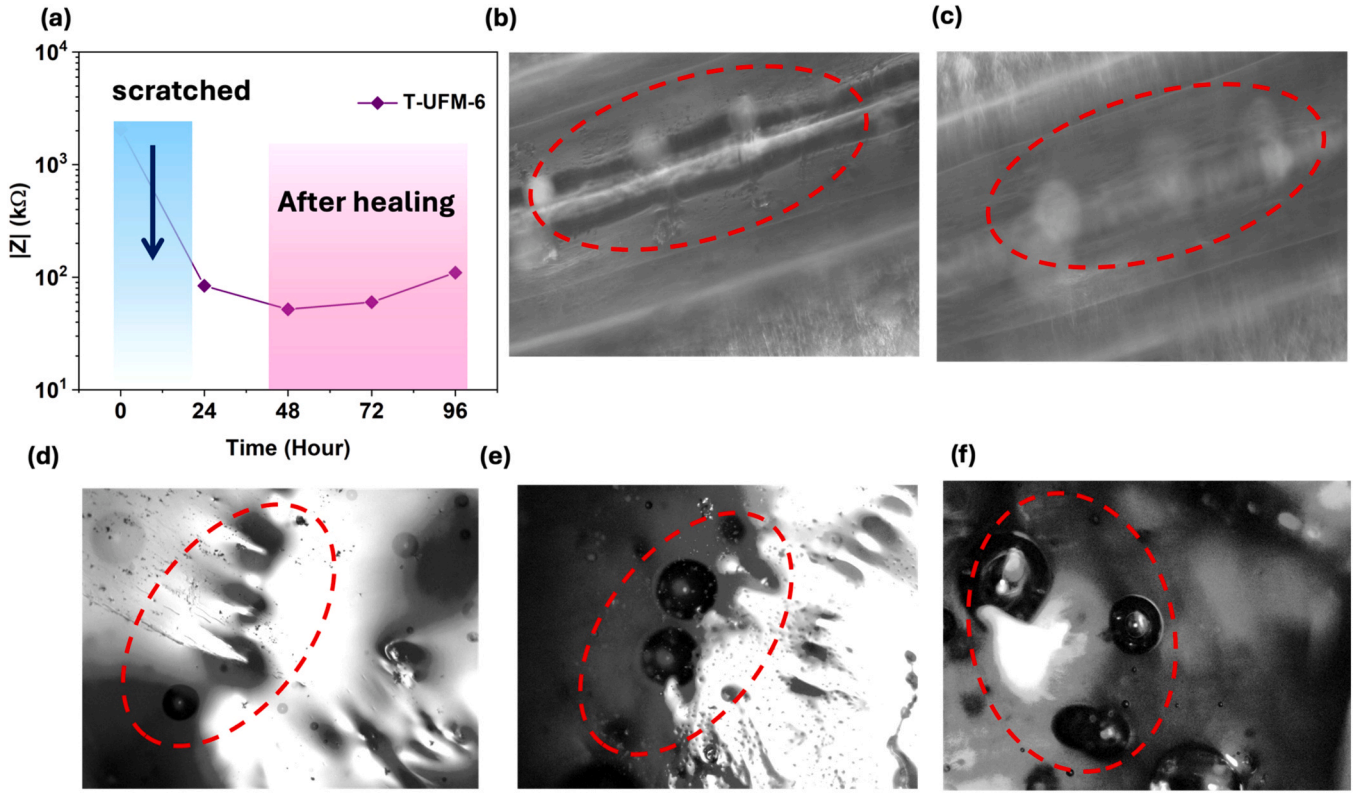

Fig. 5. **(a)** Impedance response of the T-UFM−6 coating before mechanical scratching and following 4 days of immersion in 3.5% NaCl solution, **(b)** optical images of the coating area near the damaged region, **(c)** healing of the defect, (**d,e,f**) scratched coating showing release of the healing core material at the damaged site.

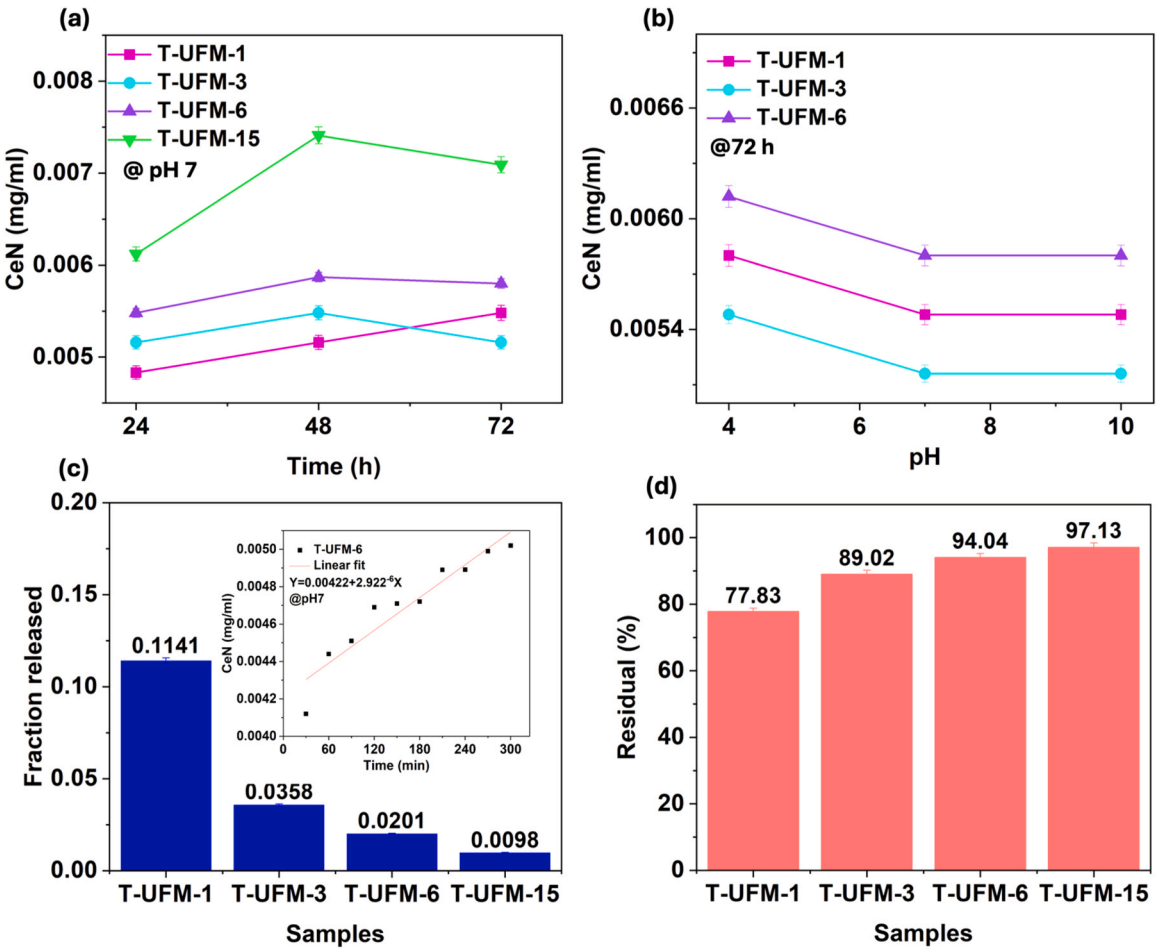

Fig. 6. The influence of time **(a)** and pH **(b)** for different coating formulations. The fraction of inhibitor release, **(c)** and residual content **(d)** for various formulations at pH 7 and after 72 h of immersion. Inset in **(c)** shows the rate of release for T-UFM−6 over the first 5 h (n = 3).

release, which is desirable for long-term corrosion protection, and this is consistent with its good corrosion protection properties, as highlighted in Fig. 3.

In Fig. 6(b), the cerium release as a function of pH is shown. All samples exhibit higher absorbance under acidic conditions, confirming that the microcapsules are pH-responsive. Optimal release occurs at mildly acidic to near-neutral pH (pH 4–6), with T-UFM−6 showing the highest release. This aligns well with corrosion-induced local acidification, which triggers the release of cerium ions, leading to the precipitation of cerium hydroxide at cathodic sites and halting the corrosion process.

The bar charts in Fig. 6(c) and (d) show the fraction of cerium released and the residual cerium levels remaining following 72 h, respectively. Based on this analysis, it is evident that the T-UFM−1 releases a large fraction of its cerium content within 72 h, and the residual concentration is low, making it unsuitable for long-term corrosion protection. Both T-UFM−3 and T-UFM−6 exhibit good release (Fig. 6(b)) and higher residual content (Fig. 6(d)), making them better suited for long-term corrosion protection. This is consistent with the data presented in Fig. 3 and Table 2, where both coatings protect the iron substrate with low corrosion currents. Although T-UFM−15 shows high overall release and high residual content, its corrosion protection properties are somewhat lower than those of T-UFM−6, indicating that the structural integrity of the coating is also an important parameter, in addition to the triggered release. This high UFM loading within the T polymer clearly affects its protective properties, which cannot be compensated for by the increased release rate of cerium and epoxy once a corrosion site is initiated.

The release kinetics of the optimised sample, T-UFM−6, were studied at pH 7 over 5 h to gain insight into the initial release. The concentration was plotted as a function of time and is shown in the inset in Fig. 6(c). A near-linear increase in cerium concentration is seen, indicating that the release follows zero-order kinetics. The cerium concentration increases gradually from about 0.00412–0.00502 mg/mL, suggesting a relatively slow release, which is beneficial for long-term corrosion protection by providing a continuous, uniform supply of the inhibitor.

A proposed mechanism is schematically shown in Scheme 2. When the T-UFM−6 coating on iron is damaged or corroded, the microcapsules at the corrosion site rupture and release their core contents, triggered by the pH change at the developing corrosion site. The trivalent cerium ions migrate to the exposed metal surface, where they react with hydroxide ions to form an adherent $Ce(OH)_3$ passive layer. This, in turn, suppresses anodic dissolution and mitigates further corrosion at the defect site. The released epoxy fills the crack and subsequently undergoes crosslinking and polymerisation, facilitated by the released cerium ions, thereby restoring the physical continuity of the coating and re-establishing its barrier properties. This healing process is further aided by the shape-memory effect of the biopolymer. This concept enables the development of smart, stimuli-responsive coatings derived from renewable polymer matrices.

To investigate the sustainability and safety of the coating system containing UFM microcapsules, the release of formaldehyde was studied daily using the Nash method according to ASTM D5910 standard. As shown in Figure S4, the T-UFM−6 coating showed no significant formaldehyde release after 7 days of immersion in PBS solution (pH 7.4) at 37 ℃, indicating good stability of the UFM capsules with negligible

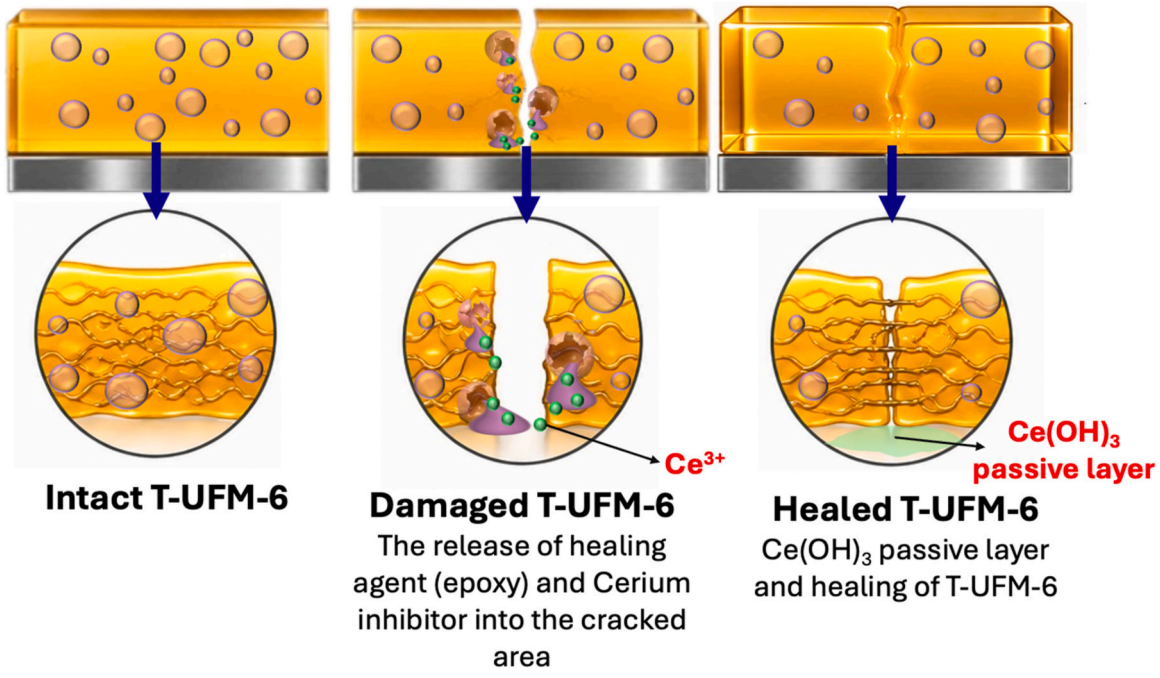

Scheme 2. Schematic representation of the healing of corrosion sites for iron modified by the T-UFM−6 coating.

formaldehyde release during the test period.

4. Conclusion

A sustainable, pH-responsive self-healing coating was developed by incorporating urea-formaldehyde microcapsules containing epoxy and cerium nitrate into a tannic acid-derived epoxy biopolymer matrix. The optimal formulation, T-UFM−6, features dual-function microcapsules that deliver both a crack-filling epoxy and an active cerium-based corrosion inhibitor promoting the epoxy polymerisation in damaged areas. This provides corrosion protection across a broad pH range and maintains the integrity of the coating. Controlled-release experiments showed that cerium nitrate is released in a pH- and time-dependent manner, with increased release observed in mildly acidic to near-neutral conditions. These release conditions are ideally suited to corrosion sites initiated by local acidification.

In addition, a substantial residual inhibitor content is retained in the capsules for continued corrosion protection. Self-healing tests in highly concentrated chloride solutions on scratched coatings confirmed that mechanical damage triggers the release of microcapsule contents, leading to crack filling by the epoxy and release of the cerium inhibitor. Overall, this work introduces a sustainable, multifunctional, bio-based coating platform that integrates passive barrier effects with smart, dual-triggered self-healing and active inhibition, and hinders the release of toxic moieties into the environment. These findings have important implications for designing responsive release systems suitable for the corrosion protection of corrosion-susceptible materials.

CRediT authorship contribution statement

Aylin Ahmadinia: Writing – original draft, Visualization, Validation, Methodology, Investigation, Formal analysis, Conceptualization. **Breslin Carmel:** Writing – review & editing, Writing – original draft, Validation, Supervision, Resources, Project administration, Funding acquisition.

Declaration of Competing Interest

The authors declare that they have no known competing financial interests or personal relationships that could have appeared to influence the work reported in this paper.

Acknowledgments

This publication has been made possible by research conducted with financial support from Research Ireland under grant number IRC/GOIPG/2023/2736. The authors would also like to acknowledge and thank Matthew Snelgrove in the Bernal Institute, University of Limerick, Ireland, for recording the XRD.

Appendix A. Supporting information

Supplementary data associated with this article can be found in the online version at doi:10.1016/j.mtcomm.2026.115667.

Data Availability

Data will be made available on request.

References

[1] I.K. Nwokolo, H. Shi, F. Liu, MOF-based protective coatings for metal corrosion protection: A critical review of design/synthesis, performance, and mechanism, Mater. Sci. Eng. B 313 (2025), https://doi.org/10.1016/j.mseb.2024.117932.
[2] D.A. Sarigiannis, S.P. Karakitsios, A. Gotti, I.L. Liakos, A. Katsoyiannis, Exposure to major volatile organic compounds and carbonyls in European indoor environments and associated health risk, Environ. Int. 37 (2011) 743–765, https://doi.org/10.1016/j.envint.2011.01.005.
[3] M. Faccini, L. Bautista, L. Soldi, A.M. Escobar, M. Altavilla, M. Calvet, A. Domènech, E. Domínguez, Environmentally friendly anticorrosive polymeric coatings, Appl. Sci. (Switz.) 11 (2021), https://doi.org/10.3390/app11083446.
[4] J. Baghdachi, Smart Coatings, UTC, 2026. ⟨https://pubs.acs.org/sharingguidelines⟩.
[5] J. Yang, T. Shen, J. Wei, C. Chen, W. Cao, W. Li, pH-responsive intrinsic self-healing coating via in-situ confined solid-liquid transition of hydrogel microdomains, NPJ Mater. Degrad. 9 (2025), https://doi.org/10.1038/s41529-025-00656-w.
[6] S. Sanyal, S.J. Park, R. Chelliah, S.J. Yeon, K. Barathikannan, S. Vijayalakshmi, Y. J. Jeong, M. Rubab, D.H. Oh, Emerging trends in smart self-healing coatings: a focus on micro/nanocontainer technologies for enhanced corrosion protection, Coatings 14 (2024), https://doi.org/10.3390/coatings14030324.

[7] Y. Zhang, M. Yu, C. Chen, S.M. Li, J.H. Liu, Self-healing coatings based on stimuli-responsive release of corrosion inhibitors: a review, Front. Mater. 8 (2022), https://doi.org/10.3389/fmats.2021.795397.
[8] A.A. Nazeer, M. Madkour, Potential use of smart coatings for corrosion protection of metals and alloys: a review, J. Mol. Liq. 253 (2018) 11–22, https://doi.org/10.1016/j.molliq.2018.01.027.
[9] K. Wang, C. Zhang, T. Zhang, K. Wang, C. Wang, H. Sun, Preparation of self-healing coatings based on pH-responsive microcapsules containing healing agents and corrosion inhibitors, Surf. Interfaces 69 (2025), https://doi.org/10.1016/j.surfin.2025.106752.
[10] A. Hasan, R. Eslami-Farsani, H. Ebrahimnezhad-Khaljiri, Effect of ZrO2 nanoparticles on the self-lubrication behavior of the linseed oil-loaded microcapsule/ epoxy composite coatings, Ceram. Int. 50 (2024) 36544–36554, https://doi.org/10.1016/j.ceramint.2024.07.039.
[11] J. Ramezanpour, R. Bagheri, S. Nouri Khorasani, B. Ramezanzadeh, M. Koochaki, Self-healing epoxy coatings filled with microcapsules of linseed oil, Mater. Chem. Phys. 350 (2026), https://doi.org/10.1016/j.matchemphys.2025.131941.
[12] Q. Yang, K. Chen, S.D.N. Lourenço, Nano-to-microscale mechanical characterization of tung oil–calcium alginate capsules for self-healing soils, Powder Technol. 469 (2026), https://doi.org/10.1016/j.powtec.2025.121906.
[13] J. Zhong, Y. Li, B. Xu, W.L. Choo, D. Wang, P. Yuan, A study on tung oil-infused polyurea microcapsules: prioritizing self-healing with bioassay-based toxicity and antibiofilm evaluations, Colloids Surf. A Physicochem. Eng. Asp. 698 (2024), https://doi.org/10.1016/j.colsurfa.2024.134529.
[14] G. Kurt Çömlekçi, S. Ulutan, Encapsulation of linseed oil and linseed oil based alkyd resin by urea formaldehyde shell for self-healing systems, Prog. Org. Coat. 121 (2018) 190–200, https://doi.org/10.1016/j.porgcoat.2018.04.027.
[15] G. Kurt Çömlekçi, S. Ulutan, Acquired self-healing ability of an epoxy coating through microcapsules having linseed oil and its alkyd, Prog. Org. Coat. 129 (2019) 292–299, https://doi.org/10.1016/j.porgcoat.2019.01.022.
[16] T. Shi, S. Livi, J. Duchet-Rumeau, J.F. Gerard, Design of self-healable epoxy-amine-ionic liquid thermosets using poly(urea- formaldehyde) microcapsules containing epoxy prepolymer, Eur. Polym. J. 215 (2024), https://doi.org/10.1016/j.eurpolymj.2024.113233.
[17] G. Perez, J.J. Gaitero, E. Erkizia, I. Jimenez, A. Guerrero, Characterisation of cement pastes with innovative self-healing system based in epoxy-amine adhesive, Cem. Concr. Compos. 60 (2015) 55–64, https://doi.org/10.1016/j.cemconcomp.2015.03.010.
[18] S. Rajasekaran, B. Huynh, S.C. Bozeman, A.P. Fugolin, Enhancing the stability of urea-formaldehyde microcapsules for self-healing polymers through additive modulation, J. Colloid Interface Sci. 704 (2026), https://doi.org/10.1016/j.jcis.2025.139454.
[19] M.J. Ramezani, O. Rahmani, H. Ebrahimnezhad-Khaljiri, Effect of graphene nanoplates in self-healing composite containing urea-formaldehyde microcapsules under tensile and interlaminar shear strength tests, Results Eng. 27 (2025), https://doi.org/10.1016/j.rineng.2025.106357.
[20] Z. Song, S. Zhang, J. Wang, Z. Huang, L. Jiang, M.Z. Guo, Y. Zhang, Preparation and self-healing properties of polyurea-MMT/HDI microcapsules for cement-based materials, J. Build. Eng. 107 (2025), https://doi.org/10.1016/j.jobe.2025.112791.
[21] J. Thakkar, N. Pandya, Pigmented epoxy polyamine self-healing coating based on polyurea-calcined fly ash-linseed oil (PU-CFA-oil) microcapsule, Mater. Lett. X 26 (2025), https://doi.org/10.1016/j.mlblux.2025.100258.
[22] P. Naghavi, R.L.M. Sofla, M. Rezaei, Z. Telikani, A.I. Ghazi-Jahani, Preparation of polyurethane shell microcapsules containing isocyanate core by Pickering emulsion method using modified silica nanoparticles and investigation of their self-healing performance, Prog. Org. Coat. 195 (2024), https://doi.org/10.1016/j.porgcoat.2024.108682.
[23] M. Zhang, R. Cong, Y. Luo, Room temperature self-healing epoxy waterborne polyurethane containing microcapsules with waterborne polyurethane shells and mercaptan cores, Mater. Adv. 3 (2022) 7015–7027, https://doi.org/10.1039/d2ma00085g.
[24] H. Huangfu, J. Duan, J. Zhang, X. Guo, Photothermal and chloride ion dual-responsive self-healing composite coating by introducing polydopamine-decorated polycaprolactone microspheres containing an imidazolium-based ionic liquid, Colloids Surf. A Physicochem. Eng. Asp. 726 (2025), https://doi.org/10.1016/j.colsurfa.2025.137880.
[25] Zheludkevich, Tedim, Freire, Fernandes, Kallip, Lisenkov, Gandini, Ferreira, Self-healing protective coatings with “green” chitosan based pre-layer reservoir of corrosion inhibitor, J. Mater. Chem. 21 (2011) 4805–4812, https://doi.org/10.1039/c1jm10304k.
[26] X. Zhao, J. Wang, H. Zhang, H. Zhang, L. Ma, X. Zhang, W. Cheng, H. Zhang, A. H. Khalaf, B. Lin, J. Tang, Self-healing performance of cellulose-based gel coating with highly loaded hybrid inhibitor, Coatings 14 (2024), https://doi.org/10.3390/coatings14070917.
[27] Akachar, AitAghzzaf, Zarki, Idouhli, Azaryouh, El Achaby, Draoui, Novel sustainable corrosion inhibitors for enhancing carbon steel corrosion resistance based on clay and lignin biopolymer extracted from raw Alfa fibers, J. Mater. Sci. 59 (2024) 17927–17944, https://doi.org/10.1007/s10853-024-09873-1.
[28] Kusmierek, Chrzescijanska, Tannic acid as corrosion inhibitor for metals and alloys, Mater. Corros. 66 (2015) 169–174, https://doi.org/10.1002/maco.201307277.
[29] J. Wang, W. Tan, H. Yang, X. Rao, X. Luo, L. Ma, C. Ren, A. Mol, D. Zhang, Towards weathering and corrosion resistant, self-warning and self-healing epoxy coatings with tannic acid loaded nanocontainers, NPJ Mater. Degrad. 7 (2023), https://doi.org/10.1038/s41529-023-00360-7.
[30] X. Sun, C. Yang, W. Zhang, J. Zheng, J. Ou, S. Ou, Toxicity of formaldehyde, and its role in the formation of harmful and aromatic compounds during food processing, Food Chem. X 25 (2025), https://doi.org/10.1016/j.fochx.2025.102225.
[31] S. Gu, H. Shi, C. Zhang, W. Wang, F. Liu, E.H. Han, Mesoporous CeO2 containers in water-borne epoxy coatings for dual active corrosion protection of mild steel, Prog. Org. Coat. 158 (2021), https://doi.org/10.1016/j.porgcoat.2021.106376.
[32] F.E.T. Heakal, O.S. Shehata, N.S. Tantawy, Enhanced corrosion resistance of magnesium alloy AM60 by cerium(III) in chloride solution, Corros. Sci. 56 (2012) 86–95, https://doi.org/10.1016/j.corsci.2011.11.019.
[33] H. Wang, R. Akid, Encapsulated cerium nitrate inhibitors to provide high-performance anti-corrosion sol-gel coatings on mild steel, Corros. Sci. 50 (2008) 1142–1148, https://doi.org/10.1016/j.corsci.2007.11.019.
[34] K. Aramaki, Self-healing protective films prepared on zinc by treatments with cerium(III) nitrate and sodium phosphate, n.d. ⟨www.elsevier.com/locate/corsci⟩.
[35] G. Farzi, A. Davoodi, A. Ahmadi, R.E. Neisiany, M.K. Anwer, M.A. Aboudzadeh, Encapsulation of cerium nitrate within Poly(urea-formaldehyde) microcapsules for the development of self-healing epoxy-based coating, ACS Omega 6 (2021) 31147–31153, https://doi.org/10.1021/acsomega.1c04597.
[36] L. Yuan, G. Liang, J.Q. Xie, L. Li, J. Guo, Preparation and characterization of poly (urea-formaldehyde) microcapsules filled with epoxy resins, Polymer (Guildf) 47 (2006) 5338–5349, https://doi.org/10.1016/j.polymer.2006.05.051.
[37] M. Bagheri Kashani, A. Salimi, M.J. Zohuriaan-Mehr, A. Hanifpour, Preparation of poly (urea-formaldehyde) microcapsules for use in capsular adhesive, J. Polym. Res. 26 (2019), https://doi.org/10.1007/s10965-019-1965-4.
[38] C. Suryanarayana, K.C. Rao, D. Kumar, Preparation and characterization of microcapsules containing linseed oil and its use in self-healing coatings, Prog. Org. Coat. 63 (2008) 72–78, https://doi.org/10.1016/j.porgcoat.2008.04.008.
[39] H.A. Shnawa, M.N. Khalaf, Y. Jahani, Thermal degradation, dynamic mechanical and morphological properties of PVC stabilized with natural polyphenol-based epoxy resin, Polym. Bull. 75 (2018) 3473–3498, https://doi.org/10.1007/s00289-017-2220-y.
[40] T. Wahyono, D.A. Astuti, I.Komang Gede Wiryawan, I. Sugoro, A. Jayanegara, Fourier Transform Mid-Infrared (FTIR) Spectroscopy to Identify Tannin Compounds in the Panicle of Sorghum Mutant Lines. IOP Conf. Ser. Mater. Sci. Eng., Institute of Physics Publishing, 2019, https://doi.org/10.1088/1757-899X/546/4/042045.
[41] H. Alhumade, H. Rezk, A.M. Nassef, M. Al-Dhaifallah, Fuzzy logic based-modeling and parameter optimization for improving the corrosion protection of stainless steel 304 by epoxy-graphene composite, IEEE Access. 7 (2019) 100899–100909, https://doi.org/10.1109/ACCESS.2019.2930902.
[42] M. Rudresh, B.H. Maruthi, K. Channakeshavalu, H.P. Nagaswarupa, Mechanical and thermal behavior of epoxy based halloysite nano clay/PMMA hybrid nanocomposites, SN Appl. Sci. 1 (2019), https://doi.org/10.1007/s42452-019-0749-0.
[43] N.A. Che Lah, P. Murthy, M.N. Mohd Zubir, The physical and optical investigations of the tannic acid functionalised Cu-based oxide nanostructures, Sci. Rep. 12 (2022), https://doi.org/10.1038/s41598-022-14281-z.
[44] M.M. Fares, S.K. Radaydeh, H.M. AlAmeen, Green tannins /Avocado oil composites; suncare and skincare materials, Arab. J. Chem. 16 (2023), https://doi.org/10.1016/j.arabjc.2023.104764.
[45] Y.M. Li, X. Miao, Z.G. Wei, J. Cui, S.Y. Li, R.M. Han, Y. Zhang, W. Wei, Iron-tannic acid nanocomplexes: facile synthesis and application for removal of methylene blue from aqueous solution, n.d.
[46] G.A. Tiruye, D. Muñoz-Torrero, T. Berthold, J. Palma, M. Antonietti, N. Fechler, R. Marcilla, Functional porous carbon nanospheres from sustainable precursors for high performance supercapacitors, J. Mater. Chem. A Mater. 5 (2017) 16263–16272, https://doi.org/10.1039/c7ta01951c.
[47] M. Liu, R.V.K.G. Thirumalai, Y. Wu, H. Wan, Characterization of the crystalline regions of cured urea formaldehyde resin, RSC Adv. 7 (2017) 49536–49541, https://doi.org/10.1039/c7ra08082d.
[48] J. Song, S. Chen, X. Yi, X. Zhao, J. Zhang, X. Liu, B. Liu, Preparation and properties of the urea-formaldehyde Res-In/Reactive halloysite nanocomposites adhesive with low-formaldehyde emission and good water resistance, Polymers (Basel) 13 (2021), https://doi.org/10.3390/polym13142224.
[49] S. Verma, M. Dhangar, H. Bajpai, K. Chaturvedi, R.K. Mohapatra, M.A. Khan, M. Azam, S.I. Al-Resayes, A.K. Srivastava, X-ray radiation shielding and microscopic studies of flexible and moldable bandage by in situ synthesized cerium oxide nanoparticles/MWCNTS nanocomposite for healthcare applications, RSC Adv. 13 (2023) 8594–8605, https://doi.org/10.1039/d3ra00067b.
[50] T. Ahamad, S.M. Alshehri, Thermal degradation and evolved gas analysis: a polymeric blend of urea formaldehyde (UF) and epoxy (DGEBA) resin, Arab. J. Chem. 7 (2014) 1140–1147, https://doi.org/10.1016/j.arabjc.2013.04.013.
[51] E. Katoueizadeh, S.M. Zebarjad, K. Janghorban, Investigating the effect of synthesis conditions on the formation of urea-formaldehyde microcapsules, J. Mater. Res. Technol. 8 (2019) 541–552, https://doi.org/10.1016/j.jmrt.2018.04.013.
[52] Z. Cheng, M. Fang, X. Chen, Y. Zhang, Y. Wang, H. Li, J. Qian, Thermal stability and flame retardancy of a cured trifunctional epoxy resin with the synergistic effects of silicon/titanium, ACS Omega 5 (2020) 4200–4212, https://doi.org/10.1021/acsomega.9b04050.
[53] W. Kiratitanavit, Z. Xia, A. Singh, R. Mosurkal, R. Nagarajan, Tann. Acid A Bio-Based Intumescent Char-Form. Addit. Nylon 6 (2016). ⟨https://www.researchgate.net/publication/305488945⟩.
[54] M. Jalalinik, S. Nickabadi, M. Askari sayar, H. Rostami, B. Golmohammadi, Enhanced structural, thermal and electrochemical properties of epoxy coatings

with UF/PFOTES- ZIF-8 self-healing microcapsules, Results Chem. 19 (2026), https://doi.org/10.1016/j.rechem.2025.102957.

[55] U. Tiringer, B. Mušič, D. Zimerl, G. Šekularac, S. Stavber, I. Milošev, The effects of cerium ions on the curing, polymerisation and condensation of hybrid sol-gel coatings, J. Non Cryst. Solids 510 (2019) 93–100, https://doi.org/10.1016/j.jnoncrysol.2018.12.021.

[56] M. Jouyandeh, M.R. Ganjali, M. Rezapour, A. Mohaddespour, K. Jabbour, H. Vahabi, N. Rabiee, S. Habibzadeh, K. Formela, M.R. Saeb, Nonisothermal cure behavior and kinetics of cerium-doped Fe3O4/epoxy nanocomposites, Appl. Organomet. Chem. 36 (2022), https://doi.org/10.1002/aoc.6825.